Split-GFP: SERS Enhancers in Plasmonic Nanocluster Probes

*Taerin Chung, Tugba Koker, and Fabien Pinaud**

The assembly of plasmonic metal nanoparticles into hot spot surface-enhanced Raman scattering (SERS) nanocluster probes is a powerful, yet challenging approach for ultrasensitive biosensing. Scaffolding strategies based on self-complementary peptides and proteins are of increasing interest for these assemblies, but the electronic and the photonic properties of such hybrid nanoclusters remain difficult to predict and optimize. Here, split-green fluorescence protein (sGFP) fragments are used as molecular glue and the GFP chromophore is used as a Raman reporter to assemble a variety of gold nanoparticle (AuNP) clusters and explore their plasmonic properties by numerical modeling. It is shown that GFP seeding of plasmonic nanogaps in AuNP/GFP hybrid nanoclusters increases near-field dipolar couplings between AuNPs and provides SERS enhancement factors above 10^8. Among the different nanoclusters studied, AuNP/GFP chains allow near-infrared SERS detection of the GFP chromophore imidazolinone/exocyclic C=C vibrational mode with theoretical enhancement factors of 10^8–10^9. For larger AuNP/GFP assemblies, the presence of non-GFP seeded nanogaps between tightly packed nanoparticles reduces near-field enhancements at Raman active hot spots, indicating that excessive clustering can decrease SERS amplifications. This study provides rationales to optimize the controlled assembly of hot spot SERS nanoprobes for remote biosensing using Raman reporters that act as molecular glue between plasmonic nanoparticles.

Dr. T. Chung, T. Koker, Dr. F. Pinaud
Department of Biological Sciences
Dana and David Dornsife College of Letters
Arts, and Sciences
University of Southern California
Los Angeles, CA 90089, USA
E-mail: pinaud@usc.edu

Dr. F. Pinaud
Department of Chemistry
Dana and David Dornsife College of Letters
Arts, and Sciences
University of Southern California
Los Angeles, CA 90089, USA

Dr. F. Pinaud
Department of Physics and Astronomy
Dana and David Dornsife College of Letters
Arts, and Sciences
University of Southern California
Los Angeles, CA 90089, USA

DOI: 10.1002/smll.201601631

1. Introduction

Chemical fingerprinting of biomolecules by Raman scattering with light is a promising approach for nondestructive and noninvasive imaging of biological samples. However, the Raman scattering of biomolecules is typically extremely weak and signals are hard to detect because of the small Raman cross section of molecules. One way to enhance the detection of Raman signals is to take advantage of surface plasmons arising at the interface between noble metals and dielectric materials.[1] Indeed, the strong evanescent electromagnetic (EM) fields occurring at the surface of metallic nanoparticles (NPs) can increase the Raman scattering of molecules positioned in very close proximity to or directly grafted on plasmonic nanomaterials by surface-enhanced Raman scattering (SERS). This SERS process and the large Raman scattering enhancements it provides for reporters encoded on metal NPs (enhancement factors of $\approx 10^2$–10^5),

has been exploited to design SERS nanotags that are used for in vivo molecular imaging, tumor targeting or single cell detection.[2–4] Even higher SERS enhancements (factors of $\approx 10^8$–10^{10}) can be achieved using colloidal plasmonic nanoclusters[5] and Raman reporters positioned within nanometer-sized gaps between two NPs or NP clusters.[6–8] When illuminated by light at appropriate wavelength and polarization state, these nanogaps provide hot spot regions where EM fields are strongly confined and sufficiently enhanced to achieve single molecule Raman detection and imaging.[9–11]

Despite their significant advantages for ultra-sensitive imaging, hot spot SERS nanocluster probes are largely underdeveloped, because forming hot spots with high selectively and stably positioning Raman reporters at these sites remains very challenging. Attempts at tackling this challenge have involved the use of NP SERS-beacons to enhance the scattering of Raman reporters upon nanoclustering with DNA scaffolds[12,13] but the formation of hot spots was not well controlled and the influence of the Raman reporters on the plasmonic properties of the NP clusters was not investigated. While nucleic acids remain the building blocks of choice for the bottom-up assembly of colloidal NPs into photonic nanomaterials,[14,15] DNA scaffolds are rapidly degraded by nucleases. Specificity and binding affinity are also anticorrelated in the 1D zipping mechanism that underlies the selective interaction between nucleic acids.[16] Both attributes limit the use of DNA scaffolds for the remote assembly of SERS nanocluster probes in vivo. In addition, nucleic acids are photonically inert biological scaffolds. They thus offer limited options for advanced photonic responses of assembled nanomaterials such as photoswitchable Raman responses and optical modulations, which could be attained if the assembled NP probes were to embody the combined photonic properties of the scaffold and those of the nanomaterial itself. An alternative approach to DNA scaffolds for the design of hot spot SERS nanocluster probes is to employ synthetic molecules that can act as molecular glue to drive the assembly of metallic NPs and the formation of nanometer size plasmonic hot spots by host–guest interactions.[17] In principle, such assembly strategies can also be implemented using self-complementary protein and peptide biomaterials, which have secondary and ternary structures that provide unmatched binding specificity and affinity in vivo (the so-called steric fit theory[18]). In particular, fluorescent proteins, which can rapidly self-assemble from highly evolved protein domain building blocks, are very good candidate for this purpose, notably because their size is small and their intrinsic and photonically active chromophore has distinct Raman signatures. Here we apply this concept by assembling a variety of gold NP (AuNP) clusters using split-green fluorescent protein (sGFP) fragments as molecular glue and we study the near-field plasmonic properties of these nanoclusters by numerical modeling.

Split-GFP fragments are complementary protein domains from a super-folder GFP that has been split into two highly asymmetric portions: a large sGFP 1–10 domain (amino acids 1–214) and a smaller sGFP 11 domain corresponding the 11th β-sheet of the super-folder GFP β-barrel[19] (M3 peptide, amino acids 215–230). Both fragments, including synthetic versions of the M3 peptide, spontaneously and irreversibly assemble in solution to form a fully folded GFP enclosing a mature chromophore. This biomolecular complementation system has been used for cell imaging,[20–24] single molecule detection in live animals,[25] cell targeting of nanomaterials,[23,26] and as a building block for supramolecular scaffolding of protein nanostructures.[27] Here, we use these sGFP fragments to drive the formation of stable nanogaps between AuNPs and to study how nanogap seeding by the assembly of sGFP fragments influences the nanophotonic properties of a variety of AuNP clusters. For this we employed 3D finite-difference time-domain (3D-FDTD) numerical modeling of EM fields that can provide detailed understandings of the subnanoscale plasmonic responses of noble metallic NPs.[28,29] Using experimental transmission electron microscopy (TEM) images for different sizes and shapes of AuNP clusters and localized mesh refinement computational techniques, we numerically observe that GFP seeding of nanogaps effectively induces the formation of plasmonic hot spots between AuNPs and additionally provides enhanced local electric field intensities at these hot spots. We show that, depending on (i) the orientation of GFP within nanogaps and on (ii) the organization of AuNPs in homo/heterodimers or higher order clusters, SERS enhancement factors that should be sufficiently large for single molecule SERS detection can be attained. Finally, through numerical investigations of a variety of nanoclusters we define a pertinent arrangement of AuNPs and GFP-seeded nanogaps to optimize SERS enhancement factors and achieve high sensitivity detection of GFP vibrational modes from sGFP-assembled AuNP nanoprobes by SERS in the near-infrared spectral range.

2. Results and Discussion

2.1. AuNP Cluster Assembly and Numerical FDTD Modeling

To form plasmonic nanoclusters by sGFP-driven assembly we functionalized AuNPs with either the large sGFP 1–10 fragment or its smaller complementary M3 peptide fragment (**Figure 1**a). sGFP 1–10 was expressed as a recombinant protein with an N-terminal tetracysteine tag allowing its oriented binding on 40 nm AuNPs. Synthetic M3 peptides with an N-terminal cysteine were used for the functionalization of AuNPs with sizes of 40, 20 or 10 nm in diameter. As observed by TEM, AuNPs modified by sGFP 1–10 or by the M3 peptide are monodispersed on their own (inset of Figure 1c and Figure S1, Supporting Information), but they assemble into nanoclusters with various sizes and shapes following coincubation (Figure 1b and Figure S1, Supporting Information). To quantify how the assembly of sGFP fragments influences the nanoscale photonic properties of different AuNP nanoclusters, we implemented FDTD modeling of their near-field plasmonic enhancements and their spectral properties.

3D-FDTD modeling was performed using the dielectric permittivity model of Au derived from Johnson and Christy[30] and a surrounding refractive index (RI) of 1.34. Based on its crystal structure,[31] GFP at the surface of AuNPs was modeled as a 2×4 nm cylindrical shape having a RI value of 1.41 (inset of Figure 1d). This RI value was

DOI: 10.1002/smll.201601631

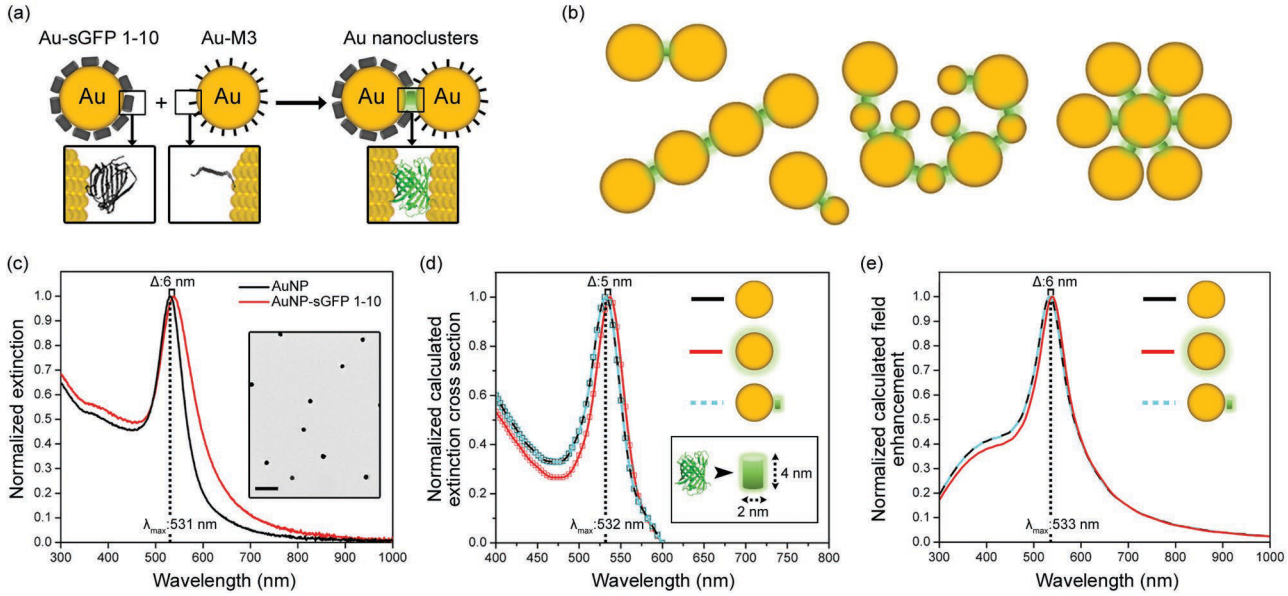

Figure 1. AuNP cluster formation and numerical FDTD modeling of GFP on AuNP monomers. a) Schematic of the formation of AuNP nanoclusters using surface-bound sGFP fragments (sGFP 1–10 and M3 peptide) as molecular glue. b) Schematic of different AuNP nanoclusters formed by sGFP-driven assembly and studied by numerical modeling. c) Experimental extinction spectra for bare 40 nm AuNPs (black) and for AuNPs coated with the large sGFP 1–10 fragment (red). Inset: TEM image of AuNPs coated with sGFP 1–10. Scale bar: 200 nm. d) Numerical modeling of the extinction spectra and e) numerical modeling of the near-field enhancement spectra for 40 nm AuNP monomers with no surface modification (black), with a monolayer coverage of sGFP 1–10 (red) and with a single sGFP 1–10 fragment attached to the surface (blue dash). Inset of (d): Schematic of a GFP molecule numerically modeled as a 4 × 2 nm cylinder having a refractive index of 1.41.

defined based on the observed 6 nm red-shift of the localized surface plasmon resonance (LSPR) peak for 40 nm AuNPs coated with a monolayer of the sGFP 1–10 fragment (Figure 1c). This red-shift is equivalent to a change in RI of about 0.07 RI units upon sGFP binding (RI sensitivity of 88 nm/RI unit, Figure S2, Supporting Information).

To validate our 3D-FDTD modeling conditions and environments, we first calculated the far-field extinction spectra and the near-field EM enhancement spectra for bare 40 nm AuNP monomers, for AuNPs coated with a monolayer of GFP (surrounding RI of 1.41) and for AuNPs with a single GFP bound to the surface (Figure 1d,e). For bare AuNP monomers, the calculated LSPR extinction peak maximum is similar to that observed experimentally (Figure 1d, λ_{max}: 532 nm) and is shifted by 5 nm when modeling a GFP monolayer coverage (Figure 1d). The RI sensitivity of the calculated LSPR peak maximum is 68 nm/RI unit, close to the value obtained analytically (Figure S2, Supporting Information). The presence of a single surface GFP does not significantly modify the LSPR peak maximum (Figure 1d, λ_{max}: 532 nm) consistent with the additive effect of local RI changes previously observed for partially coated AuNPs.[32] For calculated near-field enhancements, spectra were measured directly at the surface of AuNP monomers, parallel to the incident polarization state of the light source. The maximum near-field enhancement wavelengths (λ_{max}) follow a trend similar to that observed for calculated LSPR extinction peaks. There is a 6 nm red-shift between bare AuNPs and AuNPs coated with a GFP monolayer and no significant shift in peak position for AuNPs bearing a single surface GFP (Figure 1e, λ_{max}: 533 nm). The RI sensitivity of the electric field enhancement λ_{max} is 89 nm/RI unit, similar to that obtained analytically (Figure S2, Supporting Information). As previously shown for small AuNP monomers,[33] there is negligible red-shifting of the modeled near-field enhancement λ_{max} with respect to the far-field LSPR extinction peak maximum for bare or GFP-coated AuNPs (Figure 1d,e). Thus, our 3D-FDTD modeling parameters and environment can reproduce well the nanophotonic properties of AuNPs.

2.2. Near-Field Enhancements in sGFP-Assembled Homodimers

We then calculated the electric field enhancements for 40 nm AuNP homodimers formed by the assembly of sGFP fragments. In particular, we studied the plasmonic properties within the gap region formed by GFP at the interface between dimers by considering two possible orientations of GFP within gaps: (i) a transversal GFP orientation with a gap size of 2 nm (**Figure 2**a) and (ii) a longitudinal GFP orientation with a gap size of 4 nm (Figure 2b). Compared to AuNP monomers, extremely high field enhancements are observed for both gap sizes in homodimers and these enhanced fields are locally confined and concentrated at the location of the interfacial GFP, which forms a plasmonic hot spot (Figure 2a,b). The near-field plasmonic properties of AuNP dimers are largely dominated by this hot spot because the electric field enhancement and λ_{max} are not affected by the presence of noncomplemented sGFP 1–10 fragments at the surface of one of the AuNPs in a dimer (Figure S3, Supporting Information). As observed from the cross-sectional electric field distribution of each GFP orientation, the transverse GFP orientation (2 nm gap size, Figure 2a,c) leads to

DOI: 10.1002/smll.201601631

www.MaterialsViews.com

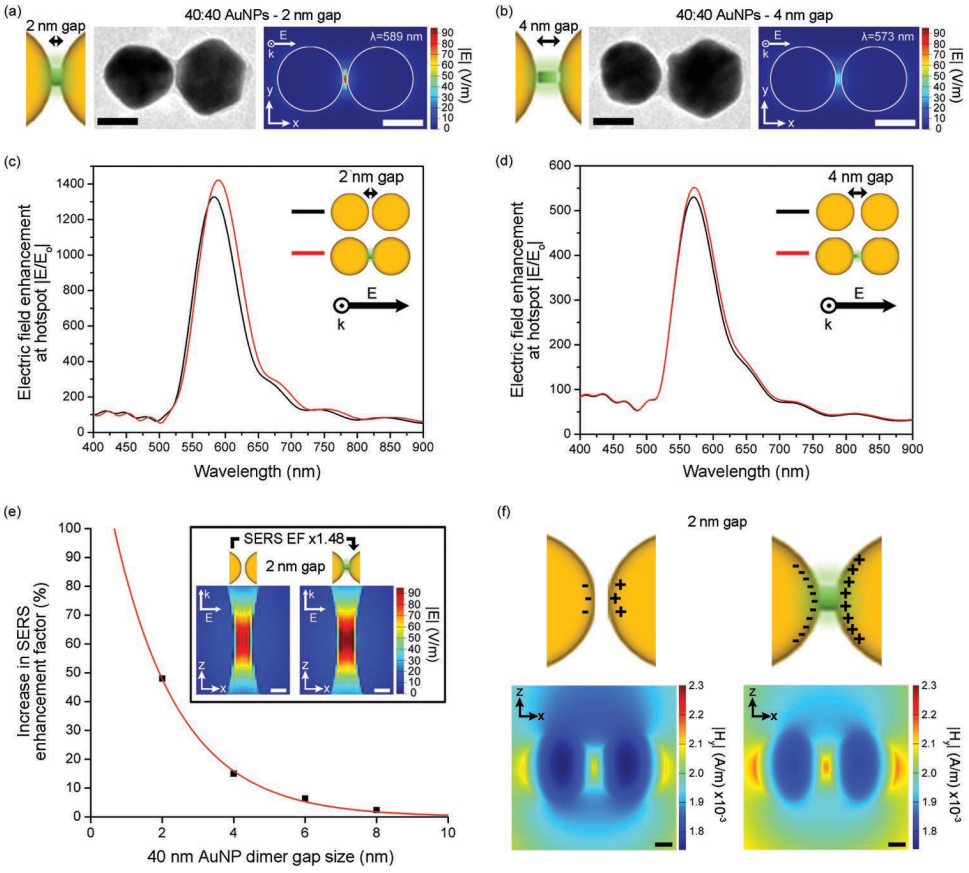

Figure 2. Numerical modeling of 40 nm AuNP homodimers assembled by sGFP fragments. a,b) Schematics, TEM images, and cross-sectional electric field enhancement distributions of homodimers formed by the 2 nm transversal or the 4 nm longitudinal orientation of GFP. Scale bars: 25 nm. c,d) Near-field enhancement spectra at hot spot for 2 or 4 nm gap homodimers with hollow (black) or GFP-seeded nanogaps (red). e) Improvement in SERS enhancement factor at different nanogap sizes for GFP-seeded homodimers compared to hollow homodimers. Inset: cross-sectional field enhancement distribution for 2 nm gap hollow and GFP-seeded dimers. Scale bars: 2 nm. f) Schematic of surface charge distribution and cross-sectional profile of the *y* component of the magnetic field for hollow and GFP-seeded homodimers with 2 nm gaps. Scale bars: 10 nm.

much larger field enhancements within the hot spot region compared to the longitudinal GFP orientation (4 nm gap size, Figure 2b,d) for incident fields polarized parallel to the long axis of the dimers. In addition, the field enhancement λ_{max} for the 2 nm gap dimers is red-shifted by 16 nm compared to the 4 nm gap dimers ($\lambda_{max:2}$ = 589 nm vs $\lambda_{max:4}$ = 573 nm, Figure 2c,d), consistent with the red-shifting of optimal enhancement wavelengths generally observed with decreasing gap sizes in AuNPs nanoantennas.[34–37] As expected, only small enhancements are observed for homodimers excited by incident fields polarized perpendicular to the long axis of dimers and there is negligible differences in hot spot field enhancement between 2 and 4 nm gap dimers (Figure S4, Supporting Information). On the contrary, for parallel polarization of the incident field, the field enhancements, including SERS enhancement factors within hot spots, decay rapidly with increasing gap size, following the characteristic gap size-dependent plasmon coupling of resonant metallic nanoantennas[38–40] (Figure S5, Supporting Information).

Interestingly, the presence of an assembled GFP between two AuNPs results in larger field enhancements within hot spots and in significant red-shifts of the enhancement λ_{max}, when compared to hollow homodimers having the same gap sizes (Figure 2c,d and inset of Figure 2e). For instance, the calculated SERS enhancement factor is 1.08×10^8 and the enhancement λ_{max} is 582 nm for a homodimer with a hollow 2 nm gap, but the enhancement factor increases to 1.60×10^8 (+48%) and the λ_{max} red-shifts to 589 nm (+7 nm) for an identical homodimer assembled with sGFP fragments (Figure 2c and Figure S5, Supporting Information). This intensification of the electric field enhancement at the plasmonic hot spot is gap-size dependent, decaying exponentially with increasing distance between dimers (Figure 2e). To define the influence of GFP on the enhancement process within plasmonic gaps, we mapped the magnetic field distribution intensity, and in particular that of the *y* component of the magnetic field $|H_y|$ which results from charge currents at the surface of dimeric metal AuNPs[41] (Figure 2f). As shown in Figure 2f, $|H_y|$ is significantly larger in homodimers formed by sGFP fragment assembly than in hollow dimers, indicating that the additional GFP-induced field enhancement results from an increased dipolar mode coupling arising from surface charge amplifications within AuNPs. This boost in electric field enhancement is observed for various RI values of the GFP patch (Figure S6, Supporting Information), suggesting that the difference in RI between the seeded plasmonic nanogap and the surrounding media allows for improved mode hybridization between AuNPs. Thus, in addition to acting as molecular

small 2016,
DOI: 10.1002/smll.201601631

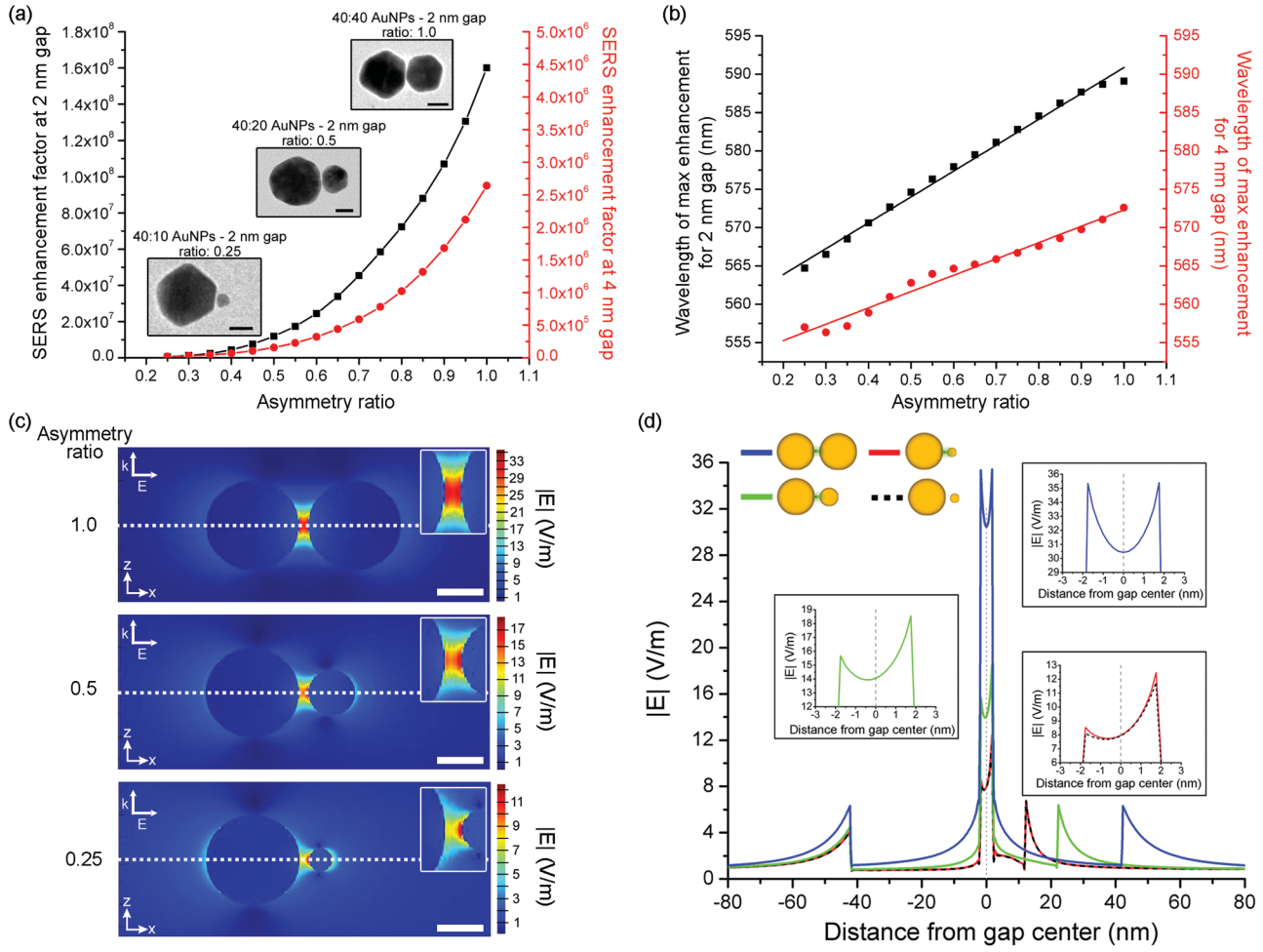

Figure 3. Numerical modeling of AuNP heterodimers assembled by sGFP fragments. a) Hot spot SERS enhancement factors as a function of asymmetry ratio for heterodimers composed of one 40 nm AuNP and formed by the 2 nm transversal or the 4 nm longitudinal orientation of GFP. Insets: TEM images of 40:40, 40:20, and 40:10 nm heterodimers. Scale bars: 20 nm. b) Shift in maximum field enhancement wavelength as a function of asymmetry ratio for heterodimers with 2 or 4 nm plasmonic gaps. c) Cross-sectional field enhancement distribution for 40:40, 40:20, and 40:10 nm heterodimers with a 4 nm longitudinal orientation of GFP. Scale bars: 20 nm. d) 1D electric field profiles along the *x*-axis of 4 nm gap heterodimers (dashed line in (c)) for GFP seeded 40:40 (blue), 40:20 (green), and 40:10 nm dimers (red) and for hollow 40:10 dimers (black dash).

glue for the formation of stable plasmonic hot spots between AuNPs, sGFP fragments also favor increased near-field coupling and increased field enhancement within plasmonic nanogaps.

2.3. Plasmonic Gap Properties of Asymmetric Heterodimers

To understand further the plasmonic responses of AuNP dimers assembled by sGFP fragments we also studied a variety of heterodimeric nanoclusters with interparticle gaps formed by the transversal or the longitudinal orientation of GFP (**Figure 3** and Figure S7, Supporting Information). Heterodimers were composed of a 40 nm AuNP coupled to AuNPs of varying sizes. For these heterodimers, the volume-integrated SERS enhancement factors within hot spot and the field enhancement λ_{max} are dependent on the size dissimilarity between the two AuNPs. For asymmetry ratios of dimers below one, SERS enhancement factors decrease exponentially with increasing asymmetry (Figure 3a), shifting from a factor of 1.60×10^8 for a 40:40 nm AuNP homodimer to a factor of 5.8×10^5 for a 10:40 nm AuNP heterodimer, in the case of 2 nm plasmonic gaps. For asymmetry ratios above one, SERS enhancement factors increase as previously reported[42] (Figure S7, Supporting Information). Gradual red-shifts of the near-field enhancement λ_{max} are also observed as symmetry increases between AuNP pairs, with, for instance, a 24 nm shift between the field enhancement λ_{max} of a 40:40 nm homodimer and that of a 10:40 nm heterodimer having 2 nm gaps (Figure 3b). Regardless of the asymmetry ratio tested, the presence of an interfacial GFP between dimers systematically leads to stronger plasmon coupling between AuNP pairs when compared to hollow dimers (Figure S7, Supporting Information). As expected, larger SERS enhancements and longer spectral red-shifts are obtained for heterodimers formed by the shorter and transversal orientation of the complemented GFP (2 nm gap, Figure 3a,b). The improved plasmonic coupling observed with increasing geometrical symmetry between AuNPs is evident from the field distribution maps of diverse dimeric

structures, which displays clear differences in electric field intensity and larger hot spot volumes with increased size similarities (Figure 3c,d). 1D field profiles also revealed that, in heterodimers, the local field intensities are not centered on the mid-gap position between dimers but are shifted toward the smaller AuNP (Figure 3d), whose increased surface curvature acts as an apex toward which propagating EM waves converge at the gap. This effect, which is similar to the light nanofocusing observed in chains of decreasing size metal NPs,[43] is likely associated with an asymmetric and polarized distribution of charges between the different size AuNPs forming the heterodimers. This slight shift in field distribution at the nanogap can reduce the excitation probability of vibrational modes of the GFP chromophore when the assembled protein, which is positioned at the center of the gap after the formation of AuNP dimers, is used as a Raman reporter. Thus, although heterodimeric AuNP nanoclusters appear of interest to lower the overall size of the dimeric complexes, their reduced plasmonic enhancement and nonsymmetric field intensity profiles is not optimal to achieved maximum SERS detection of the interfacial GFP after assembly.

2.4. Near-Field Enhancements and SERS of GFP in AuNP Chains Assembled by sGFP Fragments

In addition to forming dimers, the assembly of sGFP fragments also generates larger linear chains of 40 nm AuNPs as observed by TEM (**Figure 4**a). We thus numerically studied the plasmonic properties and the total SERS enhancements for different sizes of chains with AuNP numbers varying from n = 2–10, for gap sizes of 2 nm, and for incident fields polarized parallel to the long axis of the chains. In comparison to dimers, multiple hot spots individually positioned at plasmonic gaps between AuNPs along the chains are observed (Figure S8, Supporting Information). In these AuNP chains, the electric field enhancement is the largest at the central nanogap and its magnitude gradually decreases for nanogaps positioned at increasing distances from the chain center because dipolar plasmon mode coupling between neighbor AuNPs becomes weaker with increasing chain length[44–46] (Figures S8 and S9, Supporting Information). To calculate the total electric field enhancements emanating from different chain sizes, we summed up the hot spot-integrated SERS enhancement factors from each nanogap in a chain determined at the enhancement λ_{max} of the central and dominant nanogap. As observed for dimers, AuNP chains formed by the assembly of sGFP fragments systematically have higher SERS enhancement factors compared to identical chains with hollow gaps (Figure 4b). The total SERS enhancement factor increases more than ten folds between 40 nm homodimers (factor of 1.60×10^8) and a chain composed of four AuNPs (factor of 1.79×10^9), but rapidly levels off at a value of about 2.00×10^9 for linear chains with n = 6 AuNPs and above (Figure 4b). This large increase in total SERS enhancement for chains with n = 4 AuNPs is, in part, due to the contribution of the two surrounding nanogaps, but is primarily the result of the high electric field enhancement at the central nanogap, which stems from a reduction of nonradiative damping processes in gold as discussed below. Interestingly, as the chain grows beyond n = 4 AuNPs, the field enhancement at the central nanogap decreases gradually and becomes almost equivalent to that of the homodimers for chains with n = 10 AuNPs (Figure 4b). This local decrease, which has been previously observed for assemblies of similar size AuNP chains with nanogaps less than 3 nm,[44,46,47] is due to a volume expansion of the hybridized dipolar modes and to a larger delocalization of the field at $n > 4$. In terms of total SERS enhancement values, the reduced field intensity at the central nanogap is compensated by the accruing contribution of the surrounding nanogaps for n = 6 AuNPs, but for larger chain sizes plasmon coupling between adjacent AuNPs does not necessarily provide sufficient compensations for a significant increase in total SERS enhancement.

The strong plasmon coupling at the central nanogap for chains with n = 4 AuNPs is also accompanied by a remarkably large, 34 nm red-shift of the field enhancement λ_{max} compared to dimers ($\lambda_{max:2xAuNP}$ = 589 nm vs $\lambda_{max:4xAuNPchain}$ = 623 nm, Figure 4c,d). This extensive red-shift explains, in large part, the increase in near-field enhancement observed for n = 4 AuNP chains compared to homodimers. Indeed, for gold, nonradiative damping processes, which generally dissipate electron oscillation energy as heat, are minimized when the resonance wavelength of AuNP chains reaches a spectral range of 630–650 nm.[44] As shown in Figure 4d, the field enhancement λ_{max} for chains with n = 4 AuNPs and above rapidly reach this spectral range and SERS enhancements should be maximized with increasing numbers of AuNPs. Yet, as the number of AuNPs per chain increases to $n > 4$, the magnitude of this spectral shift decreases significantly and we observe minimal additional red-shifts of the field enhancement λ_{max} at the central hot spot which quickly converges to about 633 nm for chains with $n > 6$ AuNPs. This spectral convergence is observed for both hollow and GFP-seeded nanogaps (Figure 4d) and is primarily due to an increase in radiative damping inside the gold nanomaterial as chains are lengthened. Indeed, a close look at the near-field enhancement spectra for AuNP chains assembled by either sGFP fragments (Figure 4c) or with hollow gaps (Figure S10, Supporting Information) reveals that, in both cases, the main dipolar mode plasmon resonance band broadens as the number of AuNP per chain increases and that additional plasmon modes[45,47–49] appear as shoulders on the spectra. This band widening and the appearance of additional modes, reflect an effective rise in radiative damping along chains of increasing size which consequently leads to reduce plasmon/plasmon coupling between AuNPs, to a decrease in the amplitude of the near-field enhancements and to saturation of the spectral red-shifting. Thus, while an initial reduction in nonradiative damping favors high total SERS enhancement for short chains (n = 4–6), the increasing competitive effects of radiative damping as linear AuNP chains grow in size lead to a saturation of the total SERS enhancement factors and to the limited red-shift of the near-field resonance wavelength.

We note that the same spectral changes are also observed in numerically modeled extinction spectra of linear chains with increasing numbers of AuNPs (Figure S11, Supporting Information) in agreement with previous reports.[45,46,49]

DOI: 10.1002/smll.201601631

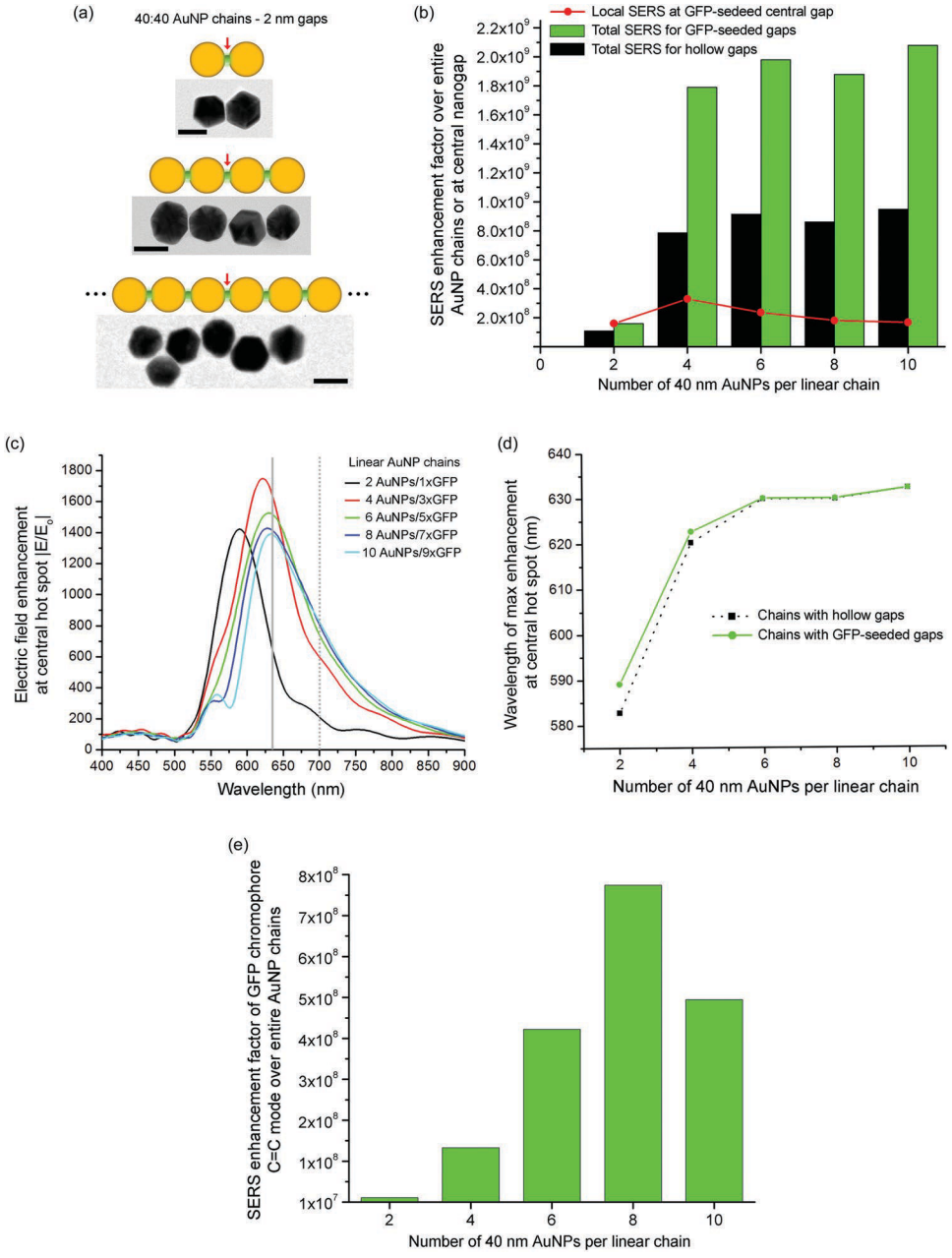

Figure 4. Numerical modeling of 40 nm AuNP linear chains with 2 nm gaps and assembled by sGFP fragments. a) Schematics and TEM images of chains with $n = 2$, $n = 4$, and $n = 6$ AuNPs. The red arrow indicates the position of the central hot spot. Scale bars: 40 nm. b) Total cumulative and central hot spot SERS enhancement factors for chains with $n = 2$ to $n = 10$ AuNPs and having hollow (black) or GFP-seeded nanogaps (green). Factors are determined at the maximum enhancement wavelength, which corresponds to the peak of the central hot spot spectra for each chains. c) Near-field enhancement spectra at the central hot spot for linear chains with AuNPs varied from $n = 2$ to $n = 10$. The position of a 633 nm laser line (gray line) and of the Stokes-shifted $\lambda_{vib\text{-}GFP}$ Raman scattered by GFP (gray dash) are also shown. d) Shift in maximum enhancement wavelength at the central hot spot for different chain sizes having hollow (black dash) or GFP seeded nanogaps (green). e) Total cumulative SERS enhancement factor of the 1530 cm^{-1} imidazolinone/exocyclic C=C vibrational mode of the GFP chromophore for an excitation at 633 nm and for chains with $n = 2$ to $n = 10$ AuNPs.

Interestingly, however, there are significant differences between the far-field extinction λ_{max} and the near-field enhancement λ_{max}, notably for the longest chains. For AuNP dimers and for chains with $n = 4$ and above, the near-field enhancement λ_{max} is blue-shifted compared to the corresponding extinction λ_{max} (Figure S11, Supporting Information), as previously observed for AuNPs forming nanogaps[50] and for some metal NP arrays.[51] For instance, while the near-field enhancement λ_{max} saturates at $\lambda \approx 633$ nm with increasing chain size, the extinction λ_{max} saturates at $\lambda \approx 700$ nm (Figure S11, Supporting Information). This shift between near- and far-field resonances has important consequences concerning the optimization of SERS signals from GFP within our sGFP-assembled AuNP nanoprobes, because it is generally assumed that the optimal SERS excitation wavelength for AuNP clusters is similar to their far-field

DOI: 10.1002/smll.201601631

resonance wavelength. While this is a reasonable assumption for AuNP dimers, it is not the case for longer chains. To assess which AuNP chain would provide, theoretically, the highest SERS enhancement of Raman-active vibrational modes for each assembled superfolder GFP within each nanogap, we calculated the total SERS enhancement factor per nanostructure at a Stokes-shifted wavelength that is Raman scattered by the GFP chromophore ($\lambda_{vib\text{-}GFP}$). In particular, we focused on the SERS enhancement of the dominant, 1530 cm^{-1} imidazolinone/exocyclic C=C vibrational mode of the chromophore,[52–54] for an excitation at 633 nm, a standard Raman laser wavelength. The total SERS enhancement was approximated as previously described[55] using

$$EF_{SERS\text{-}GFP} \approx \sum \left| \frac{E(\omega_{exc})}{E_0(\omega_{exc})} \right|^2 \left| \frac{E(\omega_{vib\text{-}GFP})}{E_0(\omega_{vib\text{-}GFP})} \right|^2 \quad (1)$$

where, for each nanogap, $E(\omega_{exc})/E_0(\omega_{exc})$ is the enhanced field at the 633 nm laser excitation and $E(\omega_{vib\text{-}GFP})/E_0(\omega_{vib\text{-}GFP})$ is the enhanced field at the Stokes-shifted wavelength of the GFP chromophore C=C mode, here 701 nm. As shown in Figure 4e, our calculations predict that the highest total SERS enhancement of the GFP chromophore is obtained for sGFP-assembled chains with $n = 8$ AuNPs, for which the C=C mode has a SERS enhancement factor of 7.75×10^8. Compared to AuNP chains with $n = 2$–6, the increased SERS enhancement at $\lambda_{vib\text{-}GFP}$ for chains with $n = 8$ AuNPs stems: (i) from the red-shift of the central hot spot plasmon band toward 633 nm which provides increased resonance (Figure 4c), (ii) from the broadening of this same band which allows better overlap with $\lambda_{vib\text{-}GFP}$ (Figure 4c), and (iii) from the cumulative effect of the surrounding hot spots whose field enhancement spectra also red-shifts toward $\lambda_{vib\text{-}GFP}$ with increasing distances from the central hot spot (Figure S9, Supporting Information). Thus, in addition to allowing detection at the onset of the near-infrared spectral region (701 nm), chains assembled with $n = 4$–10 AuNPs produce SERS enhancement factors of $\lambda_{vib\text{-}GFP}$ that are large enough for single molecule detection. This should favor high sensitivity SERS imaging of the sGFP-assembled nanoprobes in biological samples, for instance on targeted cells, if such AuNP chains are assembled in vivo.

2.5. SERS Enhancement in Large 2D Nanoclusters

The sGFP driven assembly of AuNPs also resulted in the formation of nanoclusters more complex than dimers or AuNP chains. By TEM, we observed AuNPs heptamers and, more often, a large variety of randomly organized clusters as exemplified by the ensemble of AuNP heteroclusters in Figure 5. While it is difficult to assess which nanogap is formed by sGFP assembly in symmetric heptamers with AuNPs having the same size, we attempted to evaluate the near-field distribution and the total SERS enhancement for a M3-coated central AuNP surrounded by six sGFP-coated AuNPs, all 40 nm in size (**Figure 5**a). For this specific heptamer, electric fields are not uniformly distributed when the nanostructure is excited by incident light polarized along the horizontal direction. Interparticle couplings are observed between the surrounding AuNPs and the central AuNP, but the near-field enhancements are relatively weak compared to the enhancements at gaps between the surrounding AuNPs, where most of the field enhancements appear to be positioned. The enhancement within each nanogap is also significantly lower than in dimeric AuNPs and the total SERS enhancement factor calculated for all the gaps seeded by sGFP assembly is in fact three folds less than for 40 nm homodimers (Figure 5c) as previously observed for similar nanoclusters.[56] These lower near-field enhancements are likely the result of interfering coupling modes that are typically observed in tightly coupled AuNP heptamers.[57–59]

For numerical calculations of AuNP heteroclusters formed by the assembly of 40 nm sGFP 1–10-coated AuNPs and 20 nm M3-coated AuNPs, we approximated the geometry experimentally observed by TEM, with 2 nm gap sizes for GFP-seeded nanogaps between 20 and 40 nm AuNPs and gap sizes ranging from 1 to 13 nm between other AuNPs. Together with intra-nanocluster field enhancements observed at GFP-seeded nanogaps, there are additional inter-nanocluster field

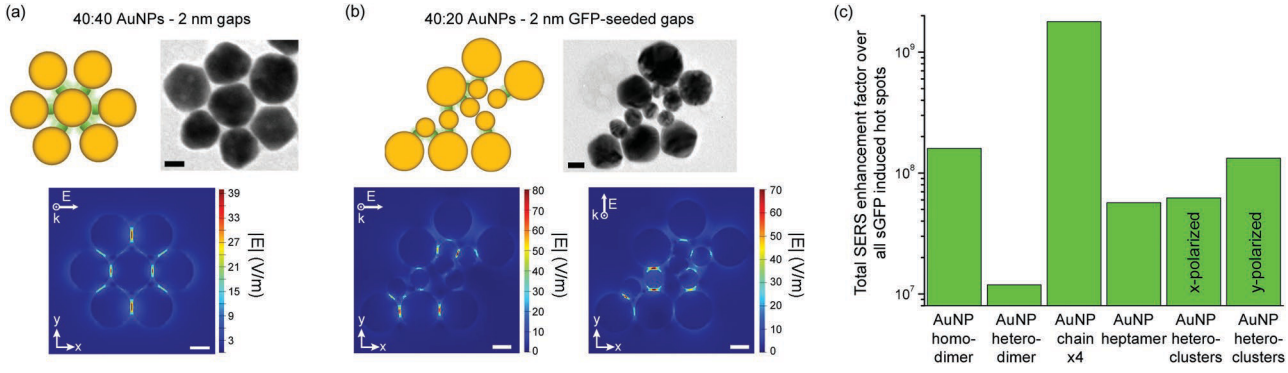

Figure 5. Modeling of complex AuNP nanoclusters assembled by sGFP fragments. Schematics, TEM images, and cross-sectional electric field enhancement distributions for a) a symmetric, 40 nm AuNP heptamer and b) a group of AuNP heteroclusters composed of one octamer and two heterodimers and formed by the assembly of 40 nm sGFP 1–10-coated AuNPs and 20 nm M3-coated AuNPs. Field enhancement distributions are presented for incident light polarized along the *x* or the *y* direction. c) Comparison of the total cumulative SERS enhancement factors over all GFP-seeded nanogaps for a variety of AuNP nanoclusters. Homodimers, chains and heptamers are formed with 40 nm AuNPs while heterodimers and heteroclusters are formed with 40 and 20 nm AuNPs. All scale bars: 20 nm.

small 2016,
DOI: 10.1002/smll.201601631

enhancements at hollow gaps between the different clusters (Figure 5b). The break in symmetry of this group of heteroclusters leads to a polarization-sensitive distribution of hotpots and SERS enhancement factors (Figure 5b,c). While this ensemble of heteroclusters provides significantly higher total SERS enhancements compared to heterodimers formed with the same AuNP sizes for both polarizations tested, the total SERS enhancement at GFP-seeded nanogaps remains lower than for homodimers or AuNPs chains (Figure 5c). Thus, depending on (i) the size of AuNPs used for the formation of nanoclusters, (ii) the cluster geometric organization, (iii) the position of GFP-seeded gaps within clusters, but also (iv) inter-nanocluster near-field interactions, total SERS enhancements can either improve or worsen. Overall, our data suggest that for AuNP nanostructures having very precise and SERS active plasmonic hot spots formed by the specific complementation of surface-attached sGFP fragments, relatively short and linear chains with n = 4–8 AuNPs 40 nm in size provide better SERS enhancement per nanostructure than larger 2D nanoclusters or than tightly packed groups of AuNP heteroclusters. In other words, if only a limited number of nanogaps are seeded with a Raman active reporter in a given AuNP nanocluster, the SERS enhancement of the reporter might not be maximized if the structure also contains hollow nanogaps, as might be expected in large NP aggregates. These observations are consistent with previous work on AuNP chains[47] and AuNP cluster arrays employed for SERS.[60]

3. Conclusion

In summary, we have shown that different types of colloidal AuNP nanoclusters can be assembled in solution using complementary sGFP fragments as molecular glue. The reconstruction of a full GFP at the interface between AuNPs not only provides means to create stable plasmonic hot spots, but also to further increase near-field couplings and SERS enhancements within nanogaps. Our numerical modeling indicate that the transversal orientation of GFP within nanogaps and the 2 nm junction it makes between NPs can provide local SERS enhancement factors above 10^8 for symmetric dimers and linear chains of 40 nm AuNPs, which is within the range generally required for high sensitivity and single molecule SERS detections. The use of smaller AuNPs as a means to assemble smaller heteromeric clusters results in lower plasmonic enhancements and in distributions of the electric field at nanogaps that do not favor high sensitivity SERS detection. This is in agreement with previous observations showing that for AuNP assemblies, notably in chains, the largest near-field enhancement are obtained with NPs 30–50 nm in diameter.[47] When considering the nonexhaustive types of sGFP-driven nanoclusters that we have studied, linear chains of AuNPs with n = 4 and above provide the highest total near-field enhancements and large red-shifts of the dipolar mode plasmon band toward resonance at 633 nm. Both effects are the consequence of the strong plasmon/plasmon coupling at GFP-seeded nanogaps between AuNPs along the chains and of the reduction of nonradiative damping processes in gold. We predict that for an excitation at 633 nm, AuNP chains with n = 8 can provide an important total Raman enhancement of the GFP chromophore imidazolinone/exocyclic C=C vibrational mode on the order of 1×10^9 folds, in the near-infrared. This enhancement factor, calculated for an idealized and perfectly ordered chain, is an estimate of the total field enhancement that the GFP chromophores might experience. Indeed, spatial disorders along the AuNP chains or additional chemical enhancements within GFP might respectively decrease or increase the SERS response of the GFP chromophore Stokes-shifted band at 1530 cm^{-1} within the chains. Our studies of more complex AuNP clusters also indicate that the formation of larger nanoclusters does not necessarily improve total GFP SERS enhancements. In fact, SERS at GFP seeded-hot spots appears to be reduced when nanostructures additionally contain non GFP-seeded hollow nanogaps that are inevitably formed as interacting AuNPs are packed into large 2D clusters other than linear chains. In this case, field couplings at non-GFP nanogaps participate in reducing plasmon couplings at GFP-seeded nanogaps. Thus, while some level of AuNP organization is required to achieve high sensitivity SERS detection of sGFP-assembled nanoclusters, excessive AuNP clustering can, in fact, lead to lower SERS enhancements. Here, we have only used spherical AuNPs but the uniform and reproducible formation of plasmonic hot spots by sGFP-driven assembly can be applied to metal NPs with different compositions and shapes such as nanorods[61] and nanoshells,[62] which could provide even larger SERS enhancements further in the near-infrared. Overall, this study provides rationales to optimize the assembly of hot spot SERS nanoprobes using Raman reporters that also act as molecular glue between plasmonic NPs. In our case, the biocompatible sGFP fragments, which act as the glue and the matured GFP chromophore, which acts as a distinct Raman reporter upon complementation, should allow controllable and remote assembly of SERS nanocluster probes on biological targets for applications such as near-infrared cell and animal bioimaging.

4. Experimental Section

sGFP Fragments and Nanoparticle Functionalization: sGFP 1–10 with an N-terminal tetracysteine tag and a 6xhis-tag sequence was expressed as a recombinant protein in *E. coli* and purified on a nickel-charged nitrilotriacetic acid column. After cleavage of the 6xhis-tag, the tetracysteine tag allows oriented binding of the sGFP 1–10 on AuNPs. The M3 fragment (New England Peptides) was obtained as a synthetic peptide with an N-terminal cysteine appended to its sequence for oriented binding on AuNPs. In a procedure that will be described in details elsewhere, 40, 20 or 10 nm citrate-capped AuNPs (Sigma-Aldrich) were functionalized with the sGFP 1–10 or the M3 peptide fragments, purified and coincubated in 8×10^{-3} M PBS buffer at pH 8.0 for 12 h. Nanoparticle clustering was verified by agarose gel electrophoresis (Figure S1, Supporting Information) and the shifted AuNP bands, corresponding to sGFP-induced AuNP nanoclusters, were electroeluted from the gel before being analyzed by TEM.

DOI: 10.1002/smll.201601631

Electron Microscopy: TEM was carried out on a JEOL JEM-2100F instrument with an acceleration voltage of 200 kV. For sample preparation, one drop of AuNP-M3, AuNP-sGFP 1–10 or AuNP reacted nanoclusters, all previously electroeluted from agarose gels in PBS was deposited on a carbon-coated copper TEM grid (200 mesh). Samples were intentionally deposited at low density to prevent the formation of drying-mediated 2D AuNP assemblies.

Extinction Measurements: Spectra of AuNP solutions were acquired on a UV–vis spectrometer (Varian Cary 50) in PBS, using a quartz cuvette with a path length of 10 mm, and a xenon flash lamp light source.

Numerical Simulations: FDTD modeling was performed on a Lumerical software package (Lumerical FDTD Solutions 8.11) using the dielectric permittivity model of Au derived from Johnson and Christy.[30] For EM calculations, Perfectly Matched Layer boundary conditions were chosen to avoid any reflections from the boundary. Normal plane light source waves defined as total-field scattered-field sources were set to be uniformly incident from the rear side of the simulation domain and had a magnitude of 1 V m^{-1}. The simulation domain ($1 \times 1 \times 1$ µm in *x*, *y*, and *z* dimensions) was set with a mesh size of 2 nm and a RI value of 1.34 corresponding to the RI of the 8×10^{-3} M PBS buffer[63] employed for the assembly of the nanoclusters. To model the nanometer size patches of assembled GFP with high precision, we inserted an additional local domain with a maximum mesh size of $1 \times 1 \times 0.4$ nm and a minimum mesh size of $0.25 \times 0.25 \times 0.25$ nm in the *x*, *y*, and *z* dimensions, respectively. The local mesh dimensions covered the entire localized plasmonic wave for each types of Au nanoclusters studied. The time-step stability factor over the physical domain was 0.99 across simulations. Field enhancements were defined as $|E/E_0|$ where E is the amplitude of the local maximum electric field and E_0 is the amplitude of the input source field, here 1 V m^{-1}. Electric fields and spectra were measured at the midgap between AuNPs. Field enhancements were reported as total integrated $|E/E_0|$ within 1D cross-sectional electric field enhancement distribution profiles. SERS enhancement factors $|E/E_0|^4$ were reported as total integrated SERS enhancements within $2 \times 2 \times 2$ nm volumes over hot spots.

Supporting Information

Supporting Information is available from the Wiley Online Library or from the author.

Acknowledgements

This work was supported by the National Science Foundation, Division of Material Research, under Grant No. 1406812. The authors thank A. M. Armani and S. Cronin for helpful discussions.

[1] W. L. Barnes, A. Dereux, T. W. Ebbesen, *Nature* **2003**, *424*, 824.
[2] J. H. Kim, J. S. Kim, H. Choi, S. M. Lee, B. H. Jun, K. N. Yu, E. Kuk, Y. K. Kim, D. H. Jeong, M. H. Cho, Y. S. Lee, *Anal. Chem.* **2006**, *78*, 6967.
[3] X. M. Qian, X. H. Peng, D. O. Ansari, Q. Yin-Goen, G. Z. Chen, D. M. Shin, L. Yang, A. N. Young, M. D. Wang, S. M. Nie, *Nat. Biotechnol.* **2008**, *26*, 83.
[4] C. L. Zavaleta, B. R. Smith, I. Walton, W. Doering, G. Davis, B. Shojaei, M. J. Natan, S. S. Gambhir, *Proc. Natl. Acad. Sci. USA* **2009**, *106*, 13511.
[5] J. M. Romo-Herrera, R. A. Alvarez-Puebla, L. M. Liz-Marzan, *Nanoscale* **2011**, *3*, 1304.
[6] S. L. Kleinman, R. R. Frontiera, A. I. Henry, J. A. Dieringer, R. P. Van Duyne, *Phys. Chem. Chem. Phys.* **2013**, *15*, 21.
[7] J. Theiss, P. Pavaskar, P. M. Echternach, R. E. Muller, S. B. Cronin, *Nano Lett.* **2010**, *10*, 2749.
[8] Y. Yokota, K. Ueno, H. Misawa, *Chem. Commun.* **2011**, *47*, 3505.
[9] K. Kneipp, Y. Wang, H. Kneipp, L. T. Perelman, I. Itzkan, R. Dasari, M. S. Feld, *Phys. Rev. Lett.* **1997**, *78*, 1667.
[10] E. C. Le Ru, P. G. Etchegoin, *Annu. Rev. Phys. Chem.* **2012**, *63*, 65.
[11] S. M. Nie, S. R. Emery, *Science* **1997**, *275*, 1102.
[12] L. Fabris, *Chem. Commun.* **2012**, *48*, 9346.
[13] X. Qian, X. Zhou, S. Nie, *J. Am. Chem. Soc.* **2008**, *130*, 14934.
[14] J. I. Cutler, E. Auyeung, C. A. Mirkin, *J. Am. Chem. Soc.* **2012**, *134*, 1376.
[15] C. A. Mirkin, *Nature* **1996**, *382*, 607.
[16] V. V. Demidov, M. D. Frank-Kamenetskii, *Trends Biochem. Sci.* **2004**, *29*, 62.
[17] R. W. Taylor, T.-C. Lee, O. A. Scherman, R. Esteban, J. Aizpurua, F. M. Huang, J. J. Baumberg, S. Mahajan, *ACS Nano* **2011**, *5*, 3878.
[18] D. E. Koshland, *Angew. Chem.-Int. Ed. Engl.* **1995**, *33*, 2375.
[19] S. Cabantous, T. C. Terwilliger, G. S. Waldo, *Nat. Biotechnol.* **2005**, *23*, 102.
[20] E. H. Feinberg, M. K. VanHoven, A. Bendesky, G. Wang, R. D. Fetter, K. Shen, C. I. Bargmannl, *Neuron* **2008**, *57*, 353.
[21] S. I. Hyun, L. Maruri-Avidal, B. Moss, *Traffic* **2015**, *16*, 787.
[22] L. Kaddoum, E. Magdeleine, G. S. Waldo, E. Joly, S. Cabantous, *BioTechniques* **2010**, *49*, 727.
[23] F. Pinaud, M. Dahan, *Proc. Natl. Acad. Sci. USA* **2011**, *108*, E201.
[24] S. B. Van Engelenburg, A. E. Palmer, *Nat. Methods* **2010**, *7*, 325.
[25] H. Zhan, R. Stanciauskas, C. Stigloher, K. K. Dizon, M. Jospin, J.-L. Bessereau, F. Pinaud, *Nat. Commun.* **2014**, *5*, 4974.
[26] S. S. Bale, S. J. Kwon, D. A. Shah, R. S. Kane, J. S. Dordick, *Biotechnol. Bioeng.* **2010**, *107*, 1040.
[27] Y. E. Kim, Y. N. Kim, J. A. Kim, H. M. Kim, Y. Jung, *Nat. Commun.* **2015**, *6*, 7134.
[28] A. S. Grimault, A. Vial, M. L. De La Chapelle, *Appl. Phys. B: Lasers Opt.* **2006**, *84*, 111.
[29] D. Radziuk, H. Moehwald, *Phys. Chem. Chem. Phys.* **2015**, *17*, 21072.
[30] P. B. Johnson, R. W. Christy, *Phys. Rev. B* **1972**, *6*, 4370.
[31] F. Yang, L. G. Moss, G. N. Phillips, *Nat. Biotechnol.* **1996**, *14*, 1246.
[32] M. Piliarik, P. Kvasnicka, N. Galler, J. R. Krenn, J. Homola, *Opt. Express* **2011**, *19*, 9213.
[33] J. Zuloaga, P. Nordlander, *Nano Lett.* **2011**, *11*, 1280.
[34] T. Chung, Y. Lim, I. M. Lee, S. Y. Lee, J. Choi, S. Roh, K. Y. Kim, B. Lee, *Opt. Express* **2011**, *19*, 20751.
[35] A. Garcia-Martin, D. R. Ward, D. Natelson, J. C. Cuevas, *Phys. Rev. B* **2011**, *83*, 193404.
[36] S. L. Kleinman, B. Sharma, M. G. Blaber, A. I. Henry, N. Valley, R. G. Freeman, M. J. Natan, G. C. Schatz, R. P. Van Duyne, *J. Am. Chem. Soc.* **2013**, *135*, 301.
[37] C. Tabor, R. Murali, M. Mahmoud, M. A. El-Sayed, *J. Phys. Chem. A* **2009**, *113*, 1946.
[38] T. Chung, S. Y. Lee, E. Y. Song, H. Chun, B. Lee, *Sensors* **2011**, *11*, 10907.
[39] E. Hao, G. C. Schatz, *J. Chem. Phys.* **2004**, *120*, 357.
[40] H. Y. Lin, C. H. Huang, C. H. Chang, Y. C. Lan, H. C. Chui, *Opt. Express* **2010**, *18*, 165.

DOI: 10.1002/smll.201601631

[41] L. Novotny, B. Hecht, *Principles of Nano-Optics*, Cambridge University Press, Cambridge, U.K. **2006**.
[42] Y. H. Zheng, L. Rosa, T. Thai, S. H. Ng, D. E. Gomez, H. Ohshima, U. Bach, *J. Mater. Chem. A* **2015**, *3*, 240.
[43] K. R. Li, M. I. Stockman, D. J. Bergman, *Phys. Rev. Lett.* **2003**, *91*, 227402.
[44] Z. B. Wang, B. S. Luk'yanchuk, W. Guo, S. P. Edwardson, D. J. Whitehead, L. Li, Z. Liu, K. G. Watkins, *J. Chem. Phys.* **2008**, *128*, 094705.
[45] L. S. Slaughter, B. A. Willingham, W.-S. Chang, M. H. Chester, N. Ogden, S. Link, *Nano Lett.* **2012**, *12*, 3967.
[46] T. Chen, M. Pourmand, A. Feizpour, B. Cushman, B. M. Reinhard, *J. Phys. Chem. Lett.* **2013**, *4*, 2147.
[47] C. Tserkezis, R. W. Taylor, J. Beitner, R. Esteban, J. J. Baumberg, J. Aizpurua, *Part. Part. Syst. Charact.* **2014**, *31*, 152.
[48] B. Willingham, S. Link, *Opt. Express* **2011**, *19*, 6450.
[49] S. J. Barrow, A. M. Funston, D. E. Gomez, T. J. Davis, P. Mulvaney, *Nano Lett.* **2011**, *11*, 4180.
[50] A. Lombardi, A. Demetriadou, L. Weller, P. Andrae, F. Benz, R. Chikkaraddy, J. Aizpurua, J. J. Baumberg, *ACS Photonics* **2016**, *3*, 471.
[51] A. D. McFarland, M. A. Young, J. A. Dieringer, R. P. Van Duyne, *J. Phys. Chem. B* **2005**, *109*, 11279.
[52] A. F. Bell, X. He, R. M. Wachter, P. J. Tonge, *Biochemistry* **2000**, *39*, 4423.
[53] S. Habuchi, M. Cotlet, R. Gronheid, G. Dirix, J. Michiels, J. Vanderleyden, F. C. De Schryver, J. Hofkens, *J. Am. Chem. Soc.* **2003**, *125*, 8446.
[54] X. He, A. F. Bell, P. J. Tonge, *J. Phys. Chem. B* **2002**, *106*, 6056.
[55] M. G. Blaber, G. C. Schatz, *Chem. Commun.* **2011**, *47*, 3769.
[56] S. Campione, S. M. Adams, R. Ragan, F. Capolino, *Opt. Express* **2013**, *21*, 7957.
[57] M. Hentschel, M. Saliba, R. Vogelgesang, H. Giessen, A. P. Alivisatos, N. Liu, *Nano Lett.* **2010**, *10*, 2721.
[58] J. B. Lassiter, H. Sobhani, J. A. Fan, J. Kundu, F. Capasso, P. Nordlander, N. J. Halas, *Nano Lett.* **2010**, *10*, 3184.
[59] J. A. Fan, C. Wu, K. Bao, J. Bao, R. Bardhan, N. J. Halas, V. N. Manoharan, P. Nordlander, G. Shvets, F. Capasso, *Science* **2010**, *328*, 1135.
[60] B. Yan, A. Thubagere, W. R. Premasiri, L. D. Ziegler, L. Dal Negro, B. M. Reinhard, *ACS Nano* **2009**, *3*, 1190.
[61] B. Nikoobakht, M. A. El-Sayed, *Chem. Mater.* **2003**, *15*, 1957.
[62] C. E. Talley, J. B. Jackson, C. Oubre, N. K. Grady, C. W. Hollars, S. M. Lane, T. R. Huser, P. Nordlander, N. J. Halas, *Nano Lett.* **2005**, *5*, 1569.
[63] L. Dieguez, N. Darwish, M. Mir, E. Martinez, M. Moreno, J. Samitier, *Sensor Lett.* **2009**, *7*, 851.

Received: May 13, 2016
Revised: June 21, 2016
Published online: